RESEARCH ARTICLE

Prediction of aerodynamic characteristics of high-lift Common Research Model in ground effect

M. Sereez[1] , N. Abramov[2] and M. Goman[2]

[1]School of Future Transport Engineering, Coventry University, Coventry, UK and [2]School of Engineering and Sustainable Development, De Montfort University, Leicester, UK
Corresponding author: M. Sereez; Email: ad8180@coventry.ac.uk

Abstract

Reynolds Averaged Navier-Stokes (RANS) simulations are performed to investigate the aerodynamic characteristics of the NASA Common Research Model (CRM) in its high-lift (HL) configuration in close proximity to the ground. The RANS simulations are conducted at a moderate Reynolds number of $Re = 5.49 \times 10^6$ and $M = 0.2$ with the use of the Spalart-Allmaras (SA) turbulence model. out of ground effect (OGE) simulation results are validated against available wind tunnel data before proceeding to in ground effect (IGE) simulations. The obtained computational results in the immediate vicinity of the ground with asymmetric aircraft attitudes demonstrate significant changes in the longitudinal and lateral-directional aerodynamic characteristics, which should be taken into account in flight dynamics analysis of aircraft during take-off and landing in crosswind conditions.

Nomenclature

CoM	reference point for aerodynamic moment
CoG	centre of gravity
c, S	wing mean aerodynamic chord length and reference area
b	wing span
C_L, C_D	lift and drag coefficient
C_N	normal force coefficient
C_l, C_m, C_n	rolling, pitching and yawing moment coefficient
Re	Reynolds number
h/c	non-dimensional vertical distance from the ground to CoG
t	physical time
U_∞	reference flow velocity

Greek symbol

α	angle-of-attack
β	sideslip angle
ϕ, θ, ψ	roll, pitch and yaw angles

1.0 Introduction

Lateral-directional aerodynamic characteristics in close proximity to the ground are important for the development of improved flight simulation during takeoff and landing in crosswind conditions. The risk

---

This paper is a version of a presentation given at the 2022 RAeS Applied Aerodynamics Conference.

of runway excursion (RE) along with approach and landing accidents can be further reduced or mitigated by incorporating the data acquired from computational and experimental investigations of ground effect aerodynamics into the improved flight dynamics models. This goal has been listed as an important research area in the Future Sky programme of the Association of European Research Establishments in Aeronautics (EREA) [1].

According to worldwide accident statistics for the commercial aircraft fleet, fatal accidents for the period 2006–2015 due to abnormal runway contact and runway excursion are second only to loss of control in flight (LOC-I) [2]. One of the effective ways to reduce such accidents during approach and landing is to train pilots on flight simulators equipped with advanced flight models that provide improved dynamics and control during the approach and landing phases [3].

Aircraft IGE aerodynamics is usually characterised by an increase in the lift coefficient C_L, a change in the pitching moment coefficient C_m in the nose-up direction and a decrease in the drag coefficient C_D. These variations are due to changes in the pressure distribution along the wing and fuselage caused by proximity to the ground and downwash transformation [4–6].

Publicly available ground effect studies with aerofoils and finite aspect ratio wings are more abundant than with full aircraft configurations [7–9]. The aerodynamics of multi-element aerofoils in close proximity to the ground shows a qualitatively different aerodynamic behaviour [4, 10–13]. Instead of an increase in the lift coefficient in close proximity to the ground, as observed for single-element aerofoils, the multi-element aerofoil 30P30N, for example, shows a noticeable drop in the lift coefficient [10, 12]. Identical lift coefficient trends from IGE simulations are also observed for the multi-element L1T2 aerofoil configuration [11]. A high-lift aerofoil in the close proximity to the ground experiences loss of the suction pressure on the upper side of the aerofoil, which are more than the increase of pressure on the lower side. The separation zone of the upper flap surface becomes more intensive and the positive ground effect is reversed by the large losses in suction pressure on the upper side [4, 13].

The impact of ground effect for a conventional transport jet with a moderate aspect ratio wing of $AR = 6$ and high-lift landing configuration was conducted in NASA using wind tunnel tests [14]. A comparison of aerodynamic characteristics was made in both free-air and close to the ground at non-dimensional height of $h/c = 0.65$. At angle-of-attack exceeding 5 degrees, the results indicated a drop in the lift coefficient C_L, rather than the generally expected increase of C_L due to positive ground effect. Based on the wind tunnel test results from Ref. [14] and other literature, an analytical model for the ground effect was formulated in a data compendium (DATCOM) report [4]. According to this report, the change of lift coefficient in close-proximity to the ground is highly dependent on the type of flaps employed. For instance, with approach to the ground, slotted flaps demonstrated a reduction of the lift coefficient C_L, while full- and partial-span split flaps indicated a minor increment in C_L.

Experimental tests for evaluation of the ground effect in a wind tunnel need a moving belt system such as employed in the German-Dutch wind tunnels (DNW) [15] for a true modelling of the runway. For example, paper [5] presents detailed wind tunnel testing for ground effect studies using a running belt system for the A320 aircraft. The presented results indicate that the close-to-ground aerodynamic characteristics of the A320 aircraft is highly dependent on the degree of flap deployment, corresponding to landing or take-off conditions. For instance, the positive ground effect associated with the usual increase of the lift coefficient diminished with larger flap deflections.

To the best of the authors' knowledge, the available data on ground effect aerodynamics corresponds only to symmetrical aircraft attitudes with zero bank angle, while landing and takeoff in crosswind conditions require aerodynamic responses to bank and yaw angles. This paper focuses on the investigation of aerodynamic characteristics of the NASA CRM [16, 17] in its wing-body high-lift (WB-HL) configuration in close proximity to the ground considering both symmetric and asymmetric aircraft attitudes. This configuration represents a typical modern transport airliner with deflected leading-edge slats and trailing-edge flaps. The Reynolds number and Mach number are taken as $Re = 5.49 \times 10^6$ and $M = 0.2$ and the height to chord ratios, characterising the closeness to the ground, as $h/c = 1.5, 1.35$ and 1.0. This corresponds to a speed of flight of $130 - 135$Kn of an aircraft landing in its high lift configuration [3]. The chosen flight conditions are identical to those used in the high-lift prediction workshop [18] to allow

comparison of the obtained simulation results with available wind tunnel and CFD data. Previously, a similar computational study of ground effect aerodynamics with non-zero bank angles was performed for a CRM in a cruise configuration [19].

The rest of the paper is organized as follows. The used computational framework including the model geometry, governing equations, boundary conditions, grid generation and numerical solver settings are presented in Section 2. The mesh independence study and validation of the obtained simulation results against experimental data corresponding to OGE conditions are shown in Section 3. The obtained OGE and IGE simulation results along with relevant discussions and post-processing analysis are presented in Section 4 and are followed by the concluding remarks in Section 5.

2.0 Computational framework

This section presents the adopted computational framework, which includes the geometry of the CRM-WB-HL configuration, methodology used for generation of the chimera/overset grids for the CRM-HL wing-body configuration and the numerical/solver setup for both IGE and OGE case studies.

2.1 Geometry and computational setup for ground effect

The geometry for the CRM-WB-HL configuration is an extension of the CRM wing-body geometry [17] also used in the Drag Prediction Workshop [20]. The CRM wing consists of a thin supercritical aerofoil with an aspect ratio of $AR = 9$ and a taper ratio of 0.25. The high-lift configuration CRM [16] that is used in this paper to estimate the ground effect is the nominal configuration provided by the High-Lift Prediction Committee in HLPW 4 [18]. The CRM-WB-HL configuration is shown in Fig. 1.

The high-lift CRM wing has the same geometrical features as the CRM wing-body configuration, with mean aerodynamic chord $c = 7.0$m, wingspan $b = 58.76$m and reference area $S_{ref} = 383.65$m^2. The inboard and outboard flaps are deflected by 40° and 37°, respectively, and the slat is deployed by 30°. Table 1 shows important reference parameters for the CRM-WB-HL configuration that was employed in this study. The original computer-aided design (CAD) model and additional geometry information are available at Refs. [16, 18, 21].

The computational domain is a virtual wind tunnel in the shape of rectangular box 1,000c away from the aircraft model CoM in every direction, except for the cases of ground effect where the negative Z direction had to be fixed in order to set up the correct non-dimensional ratio h/c defining the closeness to the ground. The usual boundary conditions used in incompressible flow simulations, i.e. the velocity inlet with fixed value boundary condition, and pressure outlet with zero gradient condition at the outlet were employed. For the wind tunnel walls, a slip boundary condition is employed while a no-slip boundary condition was used for the aircraft surfaces. In the case of close proximity to the ground, a prism boundary layer was used and a moving wall boundary condition was allocated with specified relative velocity in order to accurately capture the ground effect. In addition, for investigation of the ground effect, the desired flight attitude is obtained by rotation around the moment reference point given in Table 1. Examples of aircraft positions used to study ground effect aerodynamics with $h/c = 1.0$, $\alpha = 8.0°$ and various roll angles ϕ are shown in Fig. 2.

2.2 Governing equations

The Navier–Stokes (NS) equations governing incompressible fluid flow are the continuity and the momentum equations:

$$\nabla \cdot \mathbf{U} = 0 \tag{1}$$

$$\frac{\partial \mathbf{U}}{\partial t} + (\mathbf{U} \cdot \nabla) \, \mathbf{U} - \nu \nabla^2 \mathbf{U} = -\frac{\nabla \mathbf{p}}{\rho} \tag{2}$$
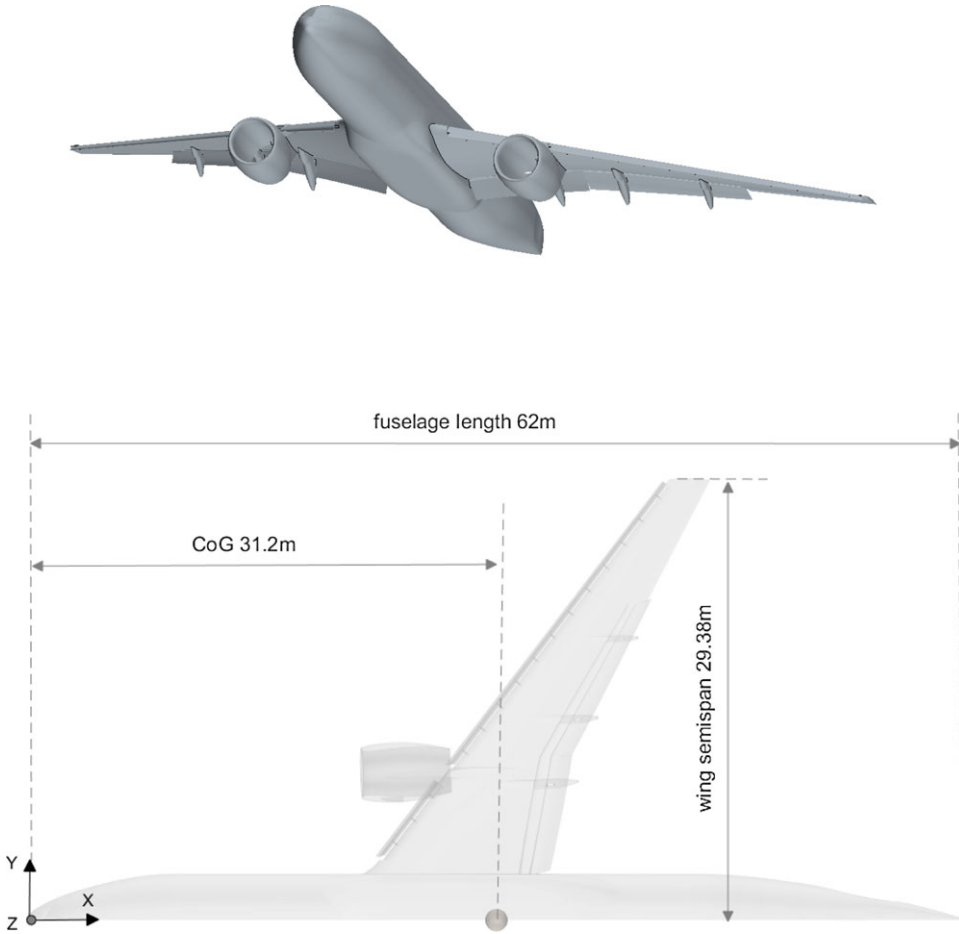
Figure 1. *Geometry of the full CRM high-lift configuration, isometric view (top) and planform view (bottom).*

where **U** is the velocity vector, ν is the kinematic viscosity of the fluid, **p** is the pressure and ρ is the density.

The computational resources required for direct numerical simulations (DNS) of Equations (1) and (2), especially for flow conditions with high Reynolds numbers, usually exceed currently available computational capabilities. Instead the RANS equations are solved, in which the Reynolds stresses arising as a result of averaging the fluctuating velocities are described by some additional empirical equations either algebraic or differential to represent an appropriate turbulence model. Most turbulence models for the RANS equations are based on the concept of eddy viscosity, which is equivalent to the kinematic viscosity of a fluid, to describe turbulent mixing or flow momentum diffusion [22]. Reynolds stresses arising in the RANS equations due to time averaging are described in linear turbulence models under the Boussinesq assumption:

$$\tau_{ij} = 2\mu_t \left(S_{ij} - \frac{1}{3} \frac{\partial u_k}{\partial x_k} \delta_{ij} \right) - \frac{2}{3} \rho k \delta_{ij} \tag{3}$$

where τ_{ij} in Equation (3) is the Reynolds stress tensor, μ_t is the turbulent viscosity, S_{ij} is the strain rate tensor and k is the kinetic energy.

Table 1. *Reference data for the CRM-WB-HL (full model)*

Wing span, b	58.76m
Mean aerodynamic chord *MAC*: c	7m
Inboard/outboard flap angles	40°/37°
Slat angle	30°
Reference area S_{ref}	383.68m²
Wing aspect ratio, *AR*	9.0
Moment reference point *CoM*	$X = 31.2$m, $\quad Y = 0, \quad Z = 4.52$m
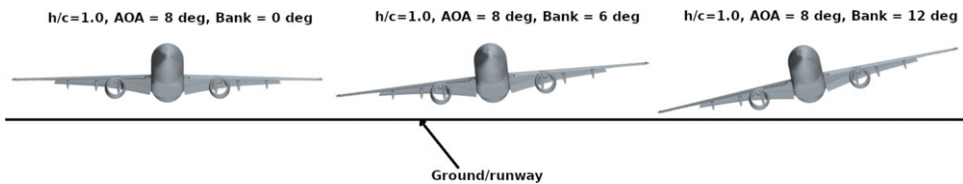
Figure 2. *Considered aircraft attitudes for investigation of the lateral-directional aerodynamics in close proximity to the ground at $h/c = 1.0$ and $\alpha = 8.0°$.*

2.3 Grid generation

Computational grids with an overset meshing approach are generated using the Siemens StarCCM+ software which is well known for its robust overset/chimera methods and simulation capabilities [23]. The reason for relying on self-generated grids rather than directly using the grids provided by HLPW [18] is twofold. Firstly, it allows to modify the flight attitudes by manipulating the overset mesh enclosing the aircraft in close proximity to the ground rather than generating/updating the grid for every new flight attitude. This is necessary as changing the wind velocity vector is not a viable option for the ground effect simulations due to the limited vertical offset distance available between the ground/runway and the velocity inlet boundary. Secondly, the overset grids also gives an opportunity to simulate the dynamic mesh for aircraft oscillatory motions for computation of dynamic aerodynamic derivatives, which is planned for a later stage of this study.

The first mesh region is taken as the overset mesh with a close-bound box around the CRM-WB-HL model 2.0m away in every direction, enabling to go for reduced proximity to the ground characterised by the non-dimensional ratio h/c. In the first mesh region, for the boundary layers generated on aircraft surface, a $Y+$ non-dimensional wall distance was chosen at a value of 1, as required in the low wall $Y+$ treatment. The second mesh region is the background mesh generated for the wind tunnel/computational domain. Further refinement or body of influence is placed in the wake of the aircraft in both the background mesh and the overset mesh region which allows to refine a region of interest in the volume mesh. Although not strictly required, conformal mesh sizes are used on the overlapping region between the overset box surface and the background mesh interface of both regions. This enables smooth interpolation of conserved flow variables between the two mesh zones. The cell area and volume in the immediate vicinity of this overlapping region or the overset interface region vary by $1 - 2\%$ between the two zones, i.e. the overset zone and the wind tunnel mesh. A coarse grid is initially generated with 5m elements. This mesh is then scaled to produce more dense and refined grid levels. The resulting computational grids are in the range of $5 - 94$m elements. The generated grid for CRM-WB-HL configuration is shown in Fig. 3.

2.4 Numerical solver settings

The numerical solver settings used in this study reflect changes in flow properties. For small angles of attack with $\alpha < 10°$, the steady RANS formulation was used along with the well-known
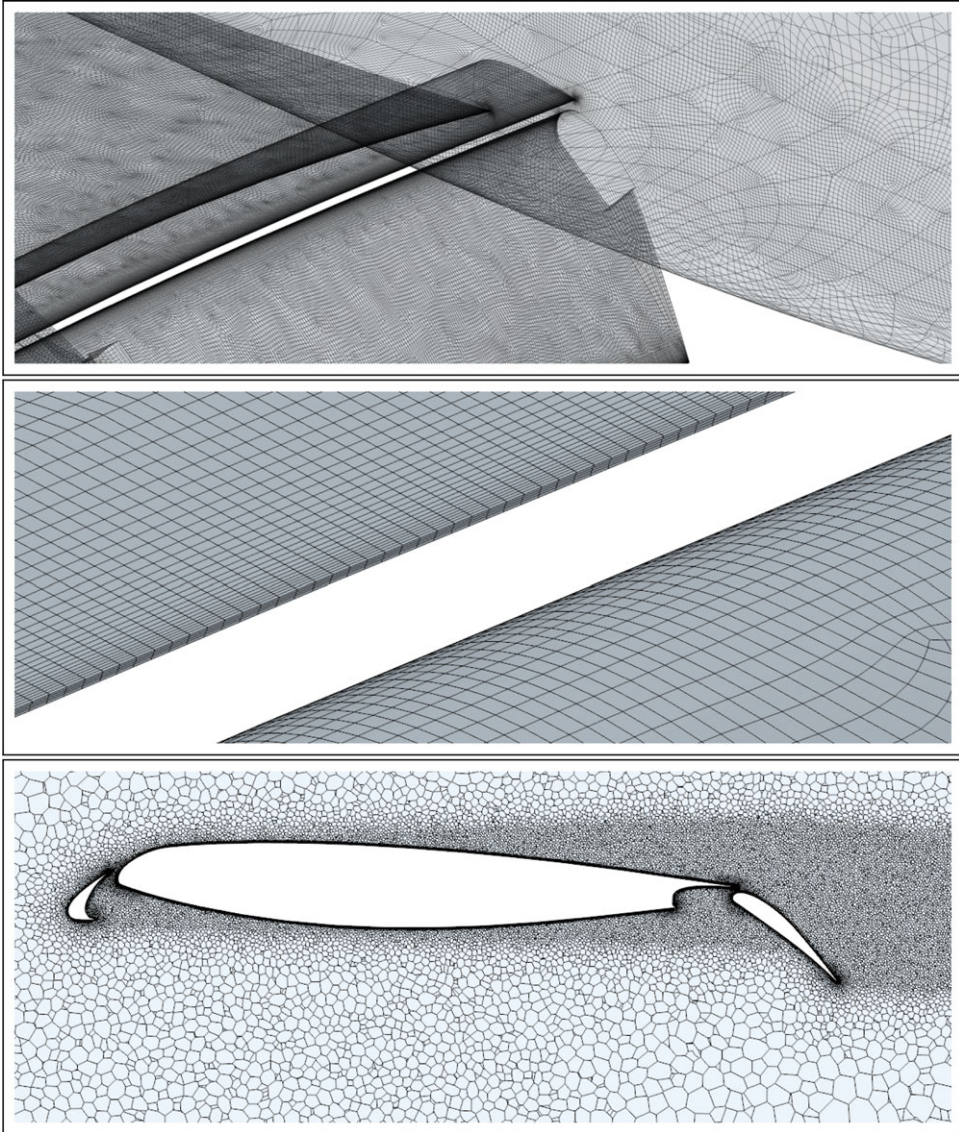
Figure 3. *Grid generated for the NASA CRM high-lift configuration, fuselage-wing connection (top), wing and flap junction (middle) and cross-sectional view of the wing (bottom) in OGE conditions.*

Spalart-Allamaras [24] turbulence model. At moderate to high angles of attack $\alpha > 10°$ the simulation was switched to the Unsteady Reynolds Averaged Navier-Stokes (URANS) formulation, as this allows a more accurate prediction of the separation zones and vortex shedding processes.

The continuity, momentum and turbulence equations were solved in a segregated manner using the algebraic multi-grid (AMG) solver with an inner tolerance of 0.001 instead of the default value of 0.1, thus solving the matrix holding the discretised finite volume coefficients to an order of a minimum three orders of magnitude. This setting allows a good convergence for every time step at the expense of slightly increased computational time. The V and F cycle approach was employed with two pre and post sweeps in order to further maximise convergence. Along with these settings, the AMG restriction tolerance was fixed at 0.9 and the prolongation tolerance was kept at 0.5. It was also necessary to exploit some degree
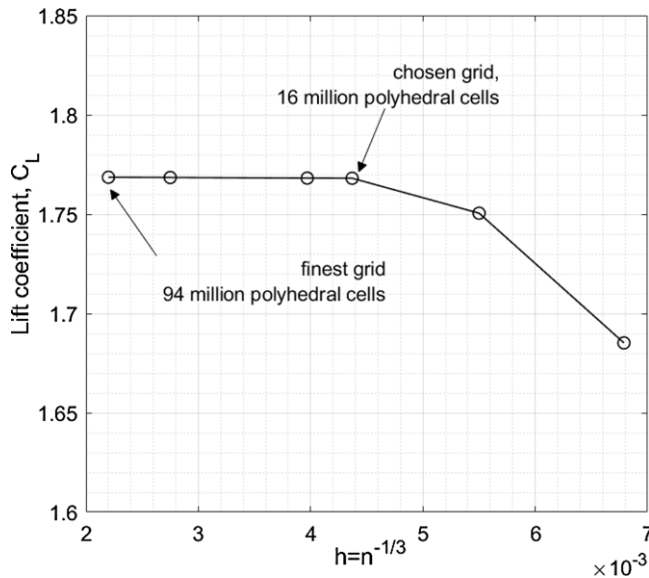
Figure 4. *Mesh independence check for OGE simulations: lift coefficient C_L at $Re = 5.49 \times 10^6$ and $M = 0.2$.*

of under-relaxation of the flow variables, especially when modelling the ground effect due to the highly non-stationary nature of the flow field.

Although the grids were intentionally constructed using a low wall $Y+$ approach, i.e. $Y+ < 1.0$, Star-CCM+ recommends using All $Y+$ treatment. With this wall treatment method, boundary layers that meets the low $Y+$ criterion are resolved using the low $Y+$ approach, and boundary layers that violate the low $Y+$ criterion are resolved using the high wall $Y+$ treatment method. The gradients of conservative flow parameters are solved with the second order of accuracy along with the Venkatakrishnan limiter [25], which excludes spurious oscillations in the flow field. The SA turbulence model was used with the rotation curvature correction option based on presentations made in Ref. [18] where this approach was shown to give good agreement with the experimental results.

3.0 Validation of the computational framework

The computational framework described above was tested in two steps. At the first stage, the simulation results were obtained with an average grid of 16×10^6 elements. Despite the fact that the region of small angles of attack, i.e. $\alpha < 10°$, was of interest, the obtained computational results were validated on wind tunnel data up to the stall angle $\alpha_s = 22.0°$.

3.1 Mesh independence check

Grid resolution plays an important role in accurately predicting aerodynamic characteristics. The six different grid levels for the CRM-WB-HL configuration were created by scaling the coarsest mesh level with approximately 5m elements. The scaling process was performed by reducing the base mesh size and increasing the resolution in the slat/wing/flap wake regions by specifying the downstream wake length and feature sizes as a percentage of the base size.

The obtained computational results for the mesh independence study at $\alpha = 7.045°$ are shown in Fig. 4. The chosen angle-of-attack at $\alpha = 7.045°$ is around the trim angle-of-attack for landing configuration which is typically in the range 0–10° for a generic transport airliner (see handling qualities data in

Table 2. *Mesh comparison for IGE and OGE conditions at $\alpha = 7.045°$ for CRM-WB-HL configuration*

h/c	Grid (no. of cells)	C_L	C_D	C_m
∞	94m	1.7685	0.1829	-0.3537
∞	16m	1.7681	0.1884	-0.3516
1.00	94m	1.7890	0.1257	-0.2611
1.00	16m	1.7825	0.1309	-0.2635

Ref. [26], p. 216). The lift coefficient C_L obtained for a grid with 16m cells is certainly independent of grid resolution, especially at such a low angle-of-attack, and therefore this level of grid resolution was chosen for study in the remaining simulations. A further mesh independence study was also conducted for IGE simulations to reassure our confidence in the chosen level of grid resolution.

The results of the grid independence study summarized in Table 2 show that at $\alpha = 7.045°$ the C_L and C_m predictions for the OGE and IGE simulations are in good agreement between the 16 and 94m elements. The drag coefficient changes more significantly with increasing grid size compared to the lift and pitching moment coefficients. However, the main focus of this study is on the lift coefficient C_L, since the rolling moment generated at the symmetric and asymmetric attitudes of the aircraft depends on the amount of lift produce by the left and right sides of the wing. Based on these results, and to minimise computational cost, a 16m mesh is used for further simulations involving ground proximity variation with zero and non-zero bank angles at various normalised height-to-chord h/c ratios from the ground.

3.2 Validation against experimental results using medium grid

The computational framework with the SA turbulence model [24] for the CRM-WB-HL model has been successfully tested against the available OGE data in a wind tunnel at Reynolds number $Re = 5.49 \times 10^6$ and Mach number $M = 0.2$ (Fig. 5). For this study, the medium grid with a total of 16m of elements was used, and the simulations were carried out on the Zeus HPC cluster facility at Coventry University [27].

The obtained computational results for the lift coefficient, drag coefficient and pitching moment coefficient are shown against the experimental data from the QinetiQ Five-Meter Pressurized Low-Speed Wind Tunnel FL4037 in Fig. 5. These wind tunnel experimental data are available to download from the HLPW site [18]. The information on the wind tunnel setup and experimental results for the high-lift configuration can be found in Ref. [21]. Figure 5 shows that the obtained computational simulation results for the lift coefficient C_L and drag coefficient C_D are in very good agreement with the experimental data at low angles of attack and in the stall region predicting quite accurately the maximum lift coefficient and the drop in the lift coefficient after the stall [18, 21]. There is a slight shift for the pitching moment coefficient C_m at low angles of attack; however, the general trend in variation of the pitching moment is captured accurately and the stall angle matches with wind tunnel data.

The WARM START simulation method in Fig. 5 refers to a technique in aerodynamic computational simulations where the converged flow field of the previous angle-of-attack's data is used as the initial solution for the flow field for simulation at a new angle-of-attack. Rather than starting from a non-converged field, the WARM START method allows to continue solution quite effectively. This technique is good for predicting the static hysteresis phenomena because the backward loop can be robustly simulated as well. The transient history of the lift coefficient C_L in the OGE simulations using the WARM START method is shown in Fig. 6.

4.0 Simulation results and discussion

This section presents the computational predictions of aerodynamic characteristics and flow field parameters obtained for the CRM-WB-HL configuration at $Re = 5.49 \times 10^6$, $M = 0.2$ and various
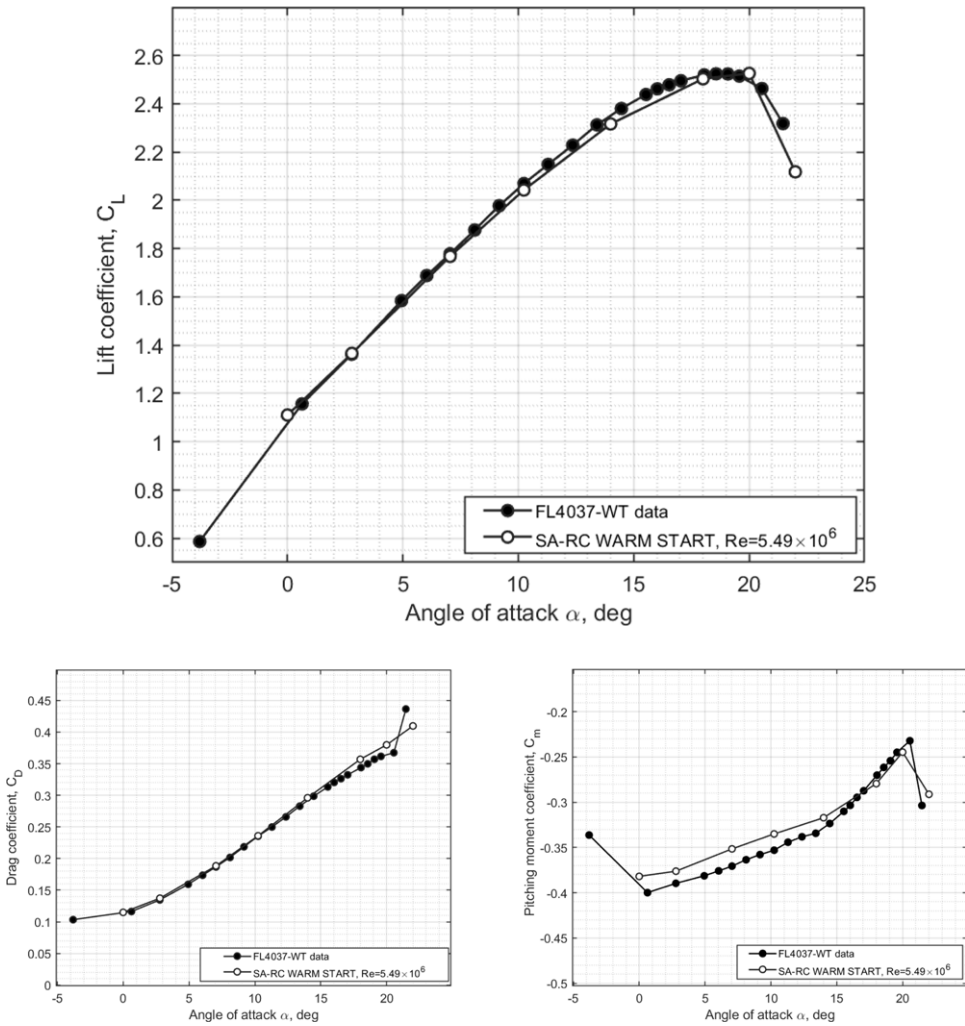
Figure 5. *Validation of CFD simulation results against the OGE wind tunnel data at $Re = 5.49 \times 10^6$ and $M = 0.2$, experimental results from Ref. [18].*
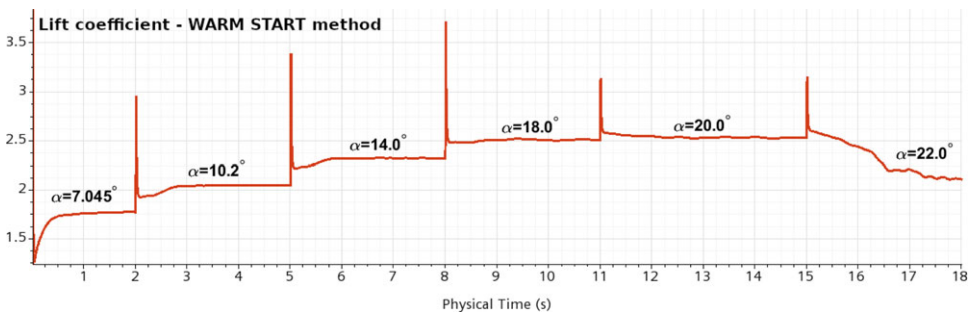

Figure 6. *Time history of the lift coefficient C_L using the WARM START method for OGE simulations at $Re = 5.49 \times 10^6$ and $M = 0.2$.*
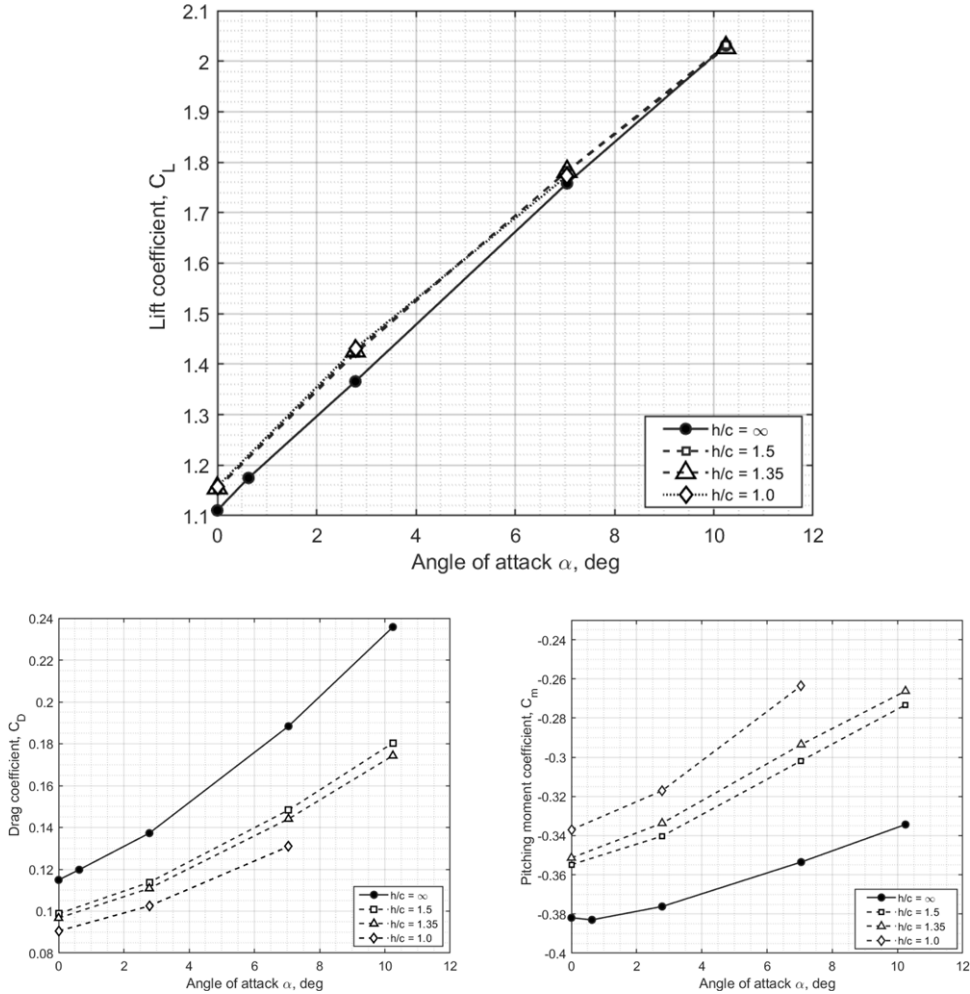
Figure 7. *Longitudinal aerodynamic characteristics for IGE simulations at $Re = 5.49 \times 10^6$, $M = 0.2$ and flaps inboard/outboard$= 40°/37°$ for $h/c = \infty$, 1.5, 1.35 and 1.0.*

height-to-chord ratios h/c. The overset mesh approach used in this study allowed simulations of IGE aerodynamics in a very close proximity to the ground and changes of aircraft attitude without mesh regeneration. Next, the results of the effect of ground on the longitudinal aerodynamic characteristics at zero bank angle are given, and followed by the effect on the lateral-directional aerodynamic coefficients at non-zero bank angles. A constant dimensionless altitude-to-chord ratio $h/c = 1.0$ is taken as the case of close proximity to the ground, and the angle-of-attack $\alpha = 8.0°$ is combined with different bank angles $\phi = 0, 4, 6, 8, 10°$. Examples of aircraft positions near the ground are shown in the Computational Framework section in Fig. 2.

4.1 Ground effect on the longitudinal aerodynamics

The simulation focuses on the analysis of the influence of the ground on the aerodynamic coefficients C_L, C_D, and C_m for various altitude-to-chord ratios. The computational results for various h/c are shown in Fig. 7. At low angles of attack $\alpha < 10°$, the maximum positive increment of the lift coefficient $\Delta C_L = 0.055$ occurs at $\alpha = 2.78°$, which is an increment of 4.029% compared with the value of the OGE.
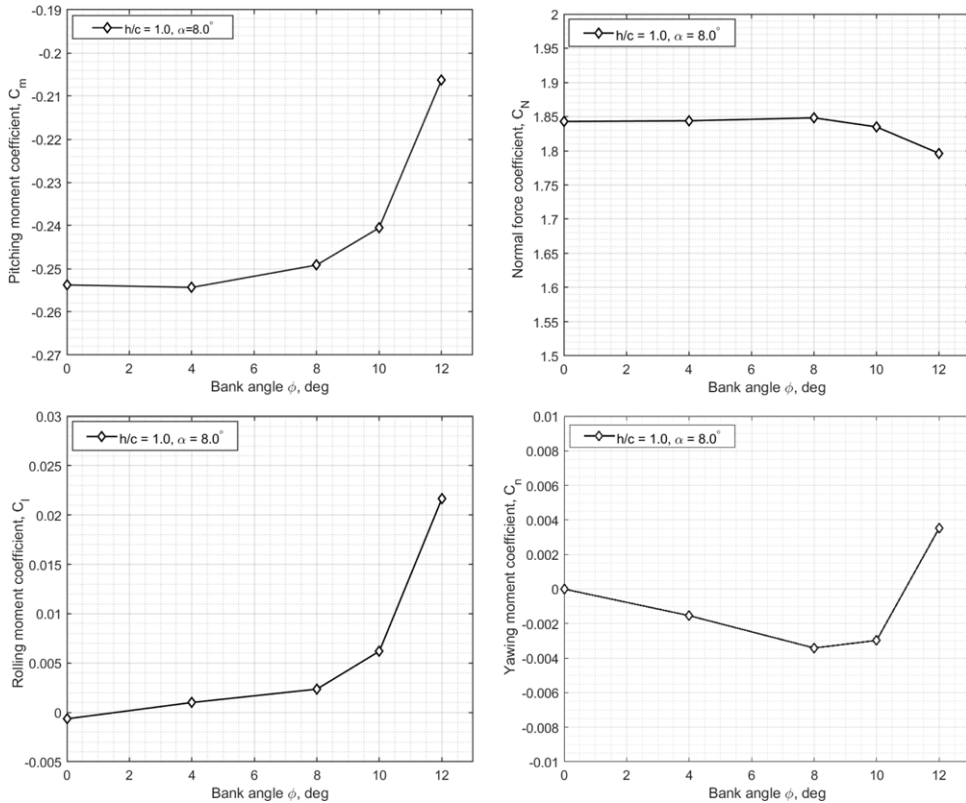
Figure 8. *Variation of aerodynamic coefficients against bank angle in IGE simulations at $\alpha = 8°$, $Re = 5.49 \times 10^6$, $M = 0.2$ and with deployment of flaps inboard/outboard at $= 40°/37°$.*

When approaching the ground, more significant changes in the coefficients of drag and pitching moment are observed. As the distance to the ground decreases from $h/c = \infty$ to $h = 1.0$, there is a significant decrease in the drag coefficient C_D and a noticeable positive increase in the pitching moment C_m. When comparing the pitching moment coefficient at $\alpha = 7.045°$ and $h/c = 1.0$ against $h/c = \infty$, an increase in the pitching moment coefficient by 25% takes place. This is a fairly noticeable change in the pitching moment and drag coefficients, which affects both the trim conditions in the longitudinal motion and the characteristics of its stability.

4.2 Ground effect on the lateral-directional aerodynamics

The simulation of the ground effect on the rolling and yawing moment coefficients is carried out by introducing a certain non-zero bank angle. When landing in a crosswind, significant bank angles will occur due to wind disturbance and the need to balance the aircraft with a non-zero bank angle (sideslip approach) [3]. Such aircraft attitudes in close proximity to the ground will induce additional changes in the rolling and yawing moments. A better understanding of flight dynamics, trimming and stability conditions in the case of crosswind landing in close proximity to the ground is an important task from the flight safety point of view [3]. The obtained simulation results for angle-of-attack $\alpha = 8.0°$ at $h/c = 1.0$ and for the range of bank angles $0° \leq \phi \leq 12°$ are presented in Fig. 8.

The simulation results in Fig. 8 show that the pitching moment coefficient C_m quite significantly increases with the bank angle in close proximity to the ground (a nose-up effect). There are very small negative changes in the normal force coefficient C_N at bank angles $\phi > 8.0°$. For example, at $\phi = 12.0°$
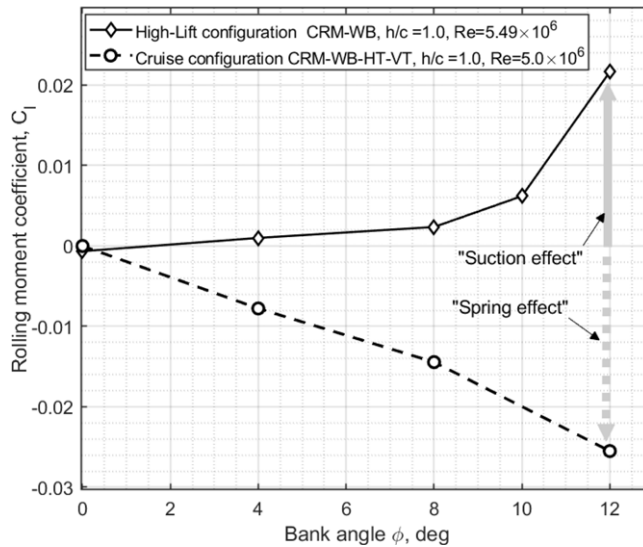
Figure 9. *Cruise vs high-lift CRM configurations: opposite trends in the rolling moment coefficient vs bank angle at* $\alpha = 8.0°$.

a decrease in the normal force coefficient C_N is equivalent to a loss of approximately 2.17% of the normal force. The percentage loss of normal force coefficient is small throughout the right wing, but increases towards the wing tip. Due to the long arm on the wing tip, the small change in the normal force generates a significant contribution to the rolling moment C_l. This effect is reflected in the rolling moment coefficient shown in Fig. 8. With the increase of bank angle ϕ (the right wing goes towards the ground) the rolling moment coefficient increases from $C_l = 0.0$ at $\phi = 0°$ to $C_l \approx 0.0218$ at $\phi = 12°$. A positive rolling moment $C_l > 0$ indicates the presence of a suction effect that presses the right wing to the ground. There is also a linear negative increment of the yawing moment coefficient C_n up until $\phi = 8.0°$ followed by a levelling off at $\phi = 10.0°$ and changing the value from negative to positive at $\phi = 12.0°$.

The results for the rolling moment coefficient versus bank angle obtained for the CRM-HL-WB configuration have the opposite trend to the cruise CRM wing-body configuration shown in Ref. [19]. On the cruise CRM configuration with an increase in the bank angle ϕ, the right wing turns to the ground, the negative rolling moments are created, forcing the right wing to push off the ground. In this case, a spring effect occurs. A comparison of the high-lift and the cruise CRM configurations is shown in Fig. 9.

To illustrate the loss of the normal force coefficient throughout the span of the wing a spanwise normal force distribution is shown in Fig. 10. The solid lines demonstrate the spanwise distribution of the normal force coefficient for the cases with $\phi = 0°$ and the dashed lines represent the cases with $\phi = 4°$ and $\phi = 10°$. It is evident that the most significant loss of the normal force occurs on the right wing. And as mentioned earlier the wing tip having the longest arm generates a significant amount of the rolling moment, see Fig. 8.

The loss of the normal force on the wing is related to the changes in the pressure on the wing surface. In order to compare the pressure coefficient distribution at a fixed location, the coefficient C_p is plotted for a cross-section cutting the wing in the x direction at 90% semi-span distance. The C_p plots are shown in Fig. 11. Blue colour-filled circle markers show the C_p for the case with zero-bank angle and the red colour-filled circles represent the C_p values for the case with bank angle $\phi = 12.0°$.

The most noticeable trend in this comparison is that the peak suction pressure on the main wing section is higher for the case with $\phi = 12.0°$ than for the case with $\phi = 0°$. However, this is only true for
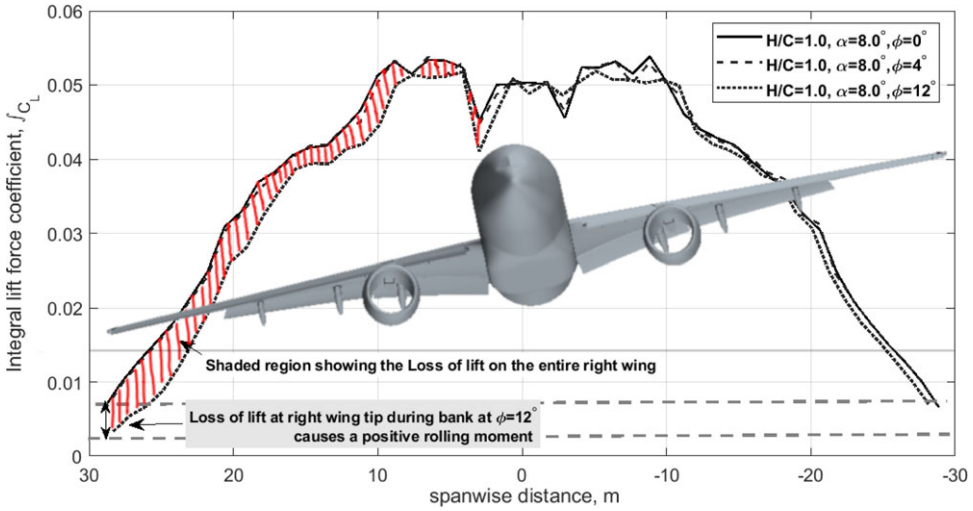
Figure 10. *Accumulated lift force coefficient in spanwise direction at different bank angles in close-proximity to the ground at $h/c = 1.0$ and $\alpha = 8.0°$.*
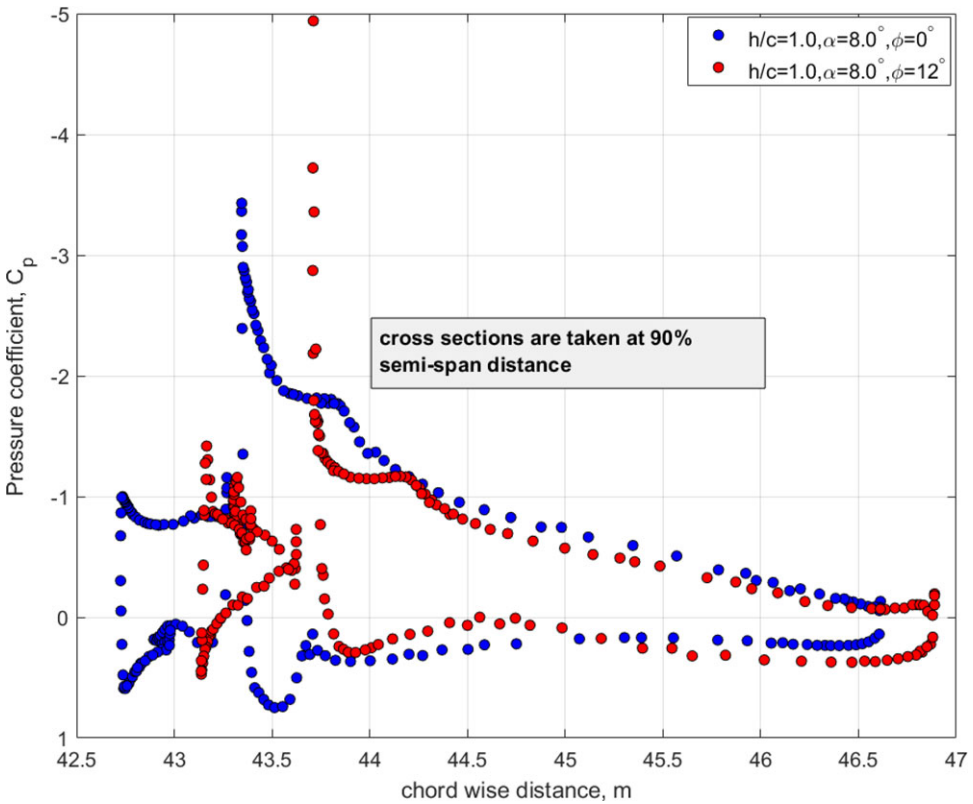

Figure 11. *Pressure coefficient C_p distributions at 90% semi-span distance for $\phi = 0°$ and $\phi = 12.0°$ in close-proximity to the ground at $h/c = 1.0$ and $\alpha = 8.0°$.*

(a)

AOA 8deg, Bank 0 deg, h/c=1.0

(b)

AOA 8deg, Bank 4 deg, h/c=1.0

(c)

AOA 8deg, Bank 8 deg, h/c=1.0

(d)

AOA 8deg, Bank 12 deg, h/c=1.0

Pressure Coefficient
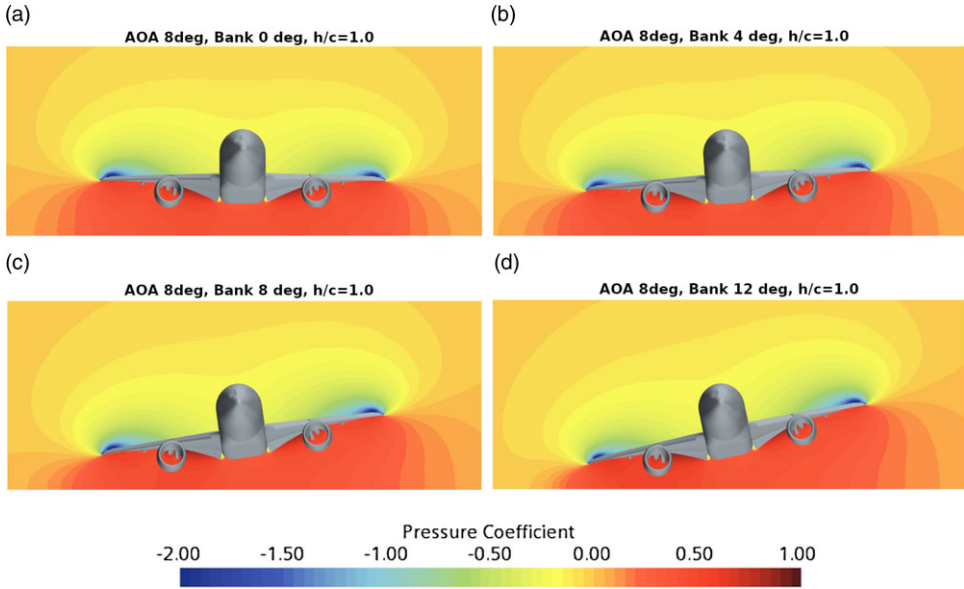
| -2.00 | -1.50 | -1.00 | -0.50 | 0.00 | 0.50 | 1.00 |

Figure 12. *Flow field pressure coefficient C_p contours in cross-section taken at $x = 37$m in different bank configurations at $\alpha = 8.0°$, $Re = 5.49 \times 10^6$, and $M = 0.2$.*

bank angle = 0 deg

bank angle = 12 deg

Skin Friction Coefficient

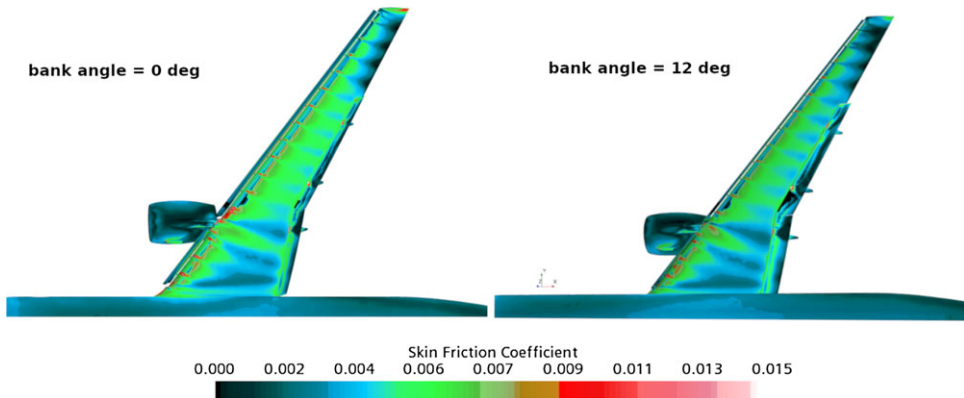| 0.000 | 0.002 | 0.004 | 0.006 | 0.007 | 0.009 | 0.011 | 0.013 | 0.015 |

Figure 13. *Skin friction coefficient C_f contours on the upper surface of the wing for different bank angles at $\alpha = 8.0°$, $Re = 5.49 \times 10^6$, and $M = 0.2$.*

a very small portion of the leading edge of the main aerofoil. It can be stated that when $\phi = 12.0°$, for the majority of the chordwise distance of the slats and the main wing section, lower positive pressure and also lower suction pressure are generated leading to an overall lower integral value of the normal force coefficient.

4.3 Post-processing of the flow field in ground effect

The analysis of the flow field is carried out using the Star-CCM+ CFD post-processing tools. Figure 12 shows the pressure coefficient contours in a plane cross-section behind the centre of gravity at $x = 37$m at a height-to-chord ratio of $h/c = 1.0$ for four different bank angles $\phi = 0, 4, 8, 12°$. When $\phi = 0°$, as expected, a symmetrical pressure coefficient distribution is observed. With the increase in bank angle,
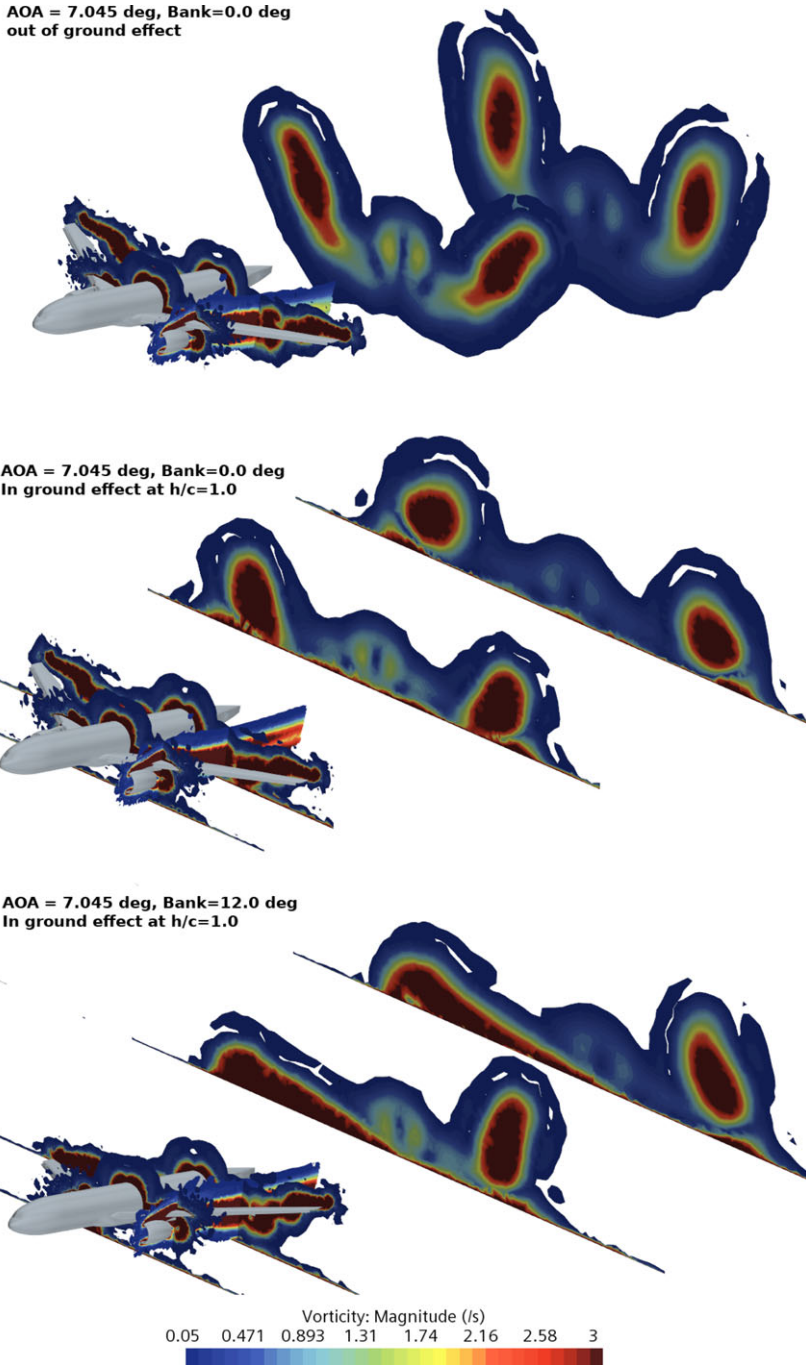
Figure 14. *Flow field vorticity contours behind the CRM-WB-HL configuration in out-of-ground and in-ground effect at* $\alpha = 7.045°$, *Re* $= 5.49 \times 10^6$, *M* $= 0.2$, *flaps inboard/outboard*$= 40°/37°$.

the high-pressure zone on the right wing side of the aircraft model reduces. This effect is maximum when $\phi = 12.0°$, leading to the loss of the normal force coefficient as seen in Fig. 8.

In Fig. 13 the skin friction coefficient C_f contours on the upper surface of the wing are shown at $h/c = 1.0$ and $\alpha = 8.0°$. The flow separation on the upper surface of the wing is more profound when $\phi = 12.0$ in comparison to the zero-bank position. More specifically there is a larger separation zone (see the black colour region in Fig. 13) towards the tip of the wing and also on the outboard flap, which also explains the loss of the normal force coefficient on the right wing (Fig. 8).

Further visualisations are carried out using vorticity contours projected on four distinct plane cross sections orthogonal to the fuselage of the aircraft in the *x*-direction and further behind downstream of the fuselage. These cross-sections are shown in Fig. 14. The changes in the vorticity and flow structure behind the wing are quite informative. When compared to the out-of-ground effect simulations, in close proximity to the ground at $h/c = 1.0$ the size of the two counter-rotating vortices which are shed behind the plane decreases in their radial circumference and maintains structure but does not get distorted. The influence of downwash is quite clear in this process. At $h/c = 1.0$ the vortex pair on the two sides are no longer identical and more interestingly, the vortex behind the right wing has broken down and deformed into a stretched but high-intensity vorticity zone. At this point, it is clear that the vortex formation and their topology during the ground effect phenomenon is certainly different from that of out-of-ground effect simulations, a deeper and detailed conclusion needs further investigation.

5.0 Concluding remarks

The presented computational predictions of the longitudinal and lateral-directional aerodynamics of the NASA high-lift CRM configuration for assessing the ground effect allow us to draw the following conclusions:

- The simulation results for the longitudinal characteristics in aircraft symmetric attitudes were validated against the experimental data from the QinetiQ Five-Meter Pressurized Low-Speed Wind Tunnel FL4037 without the effect of the ground and showed very good agreement at low angles of attack and in the stall region.
- Simulations of the ground effect at non-zero bank angles have demonstrated the presence of significant changes in the rolling and yawing moment coefficients, which can critically affect the lateral-directional stability and controllability of the aircraft during crosswind landings.

The adopted computational framework can be utilised to generate a complete set of aerodynamic coefficients, including dynamic stability derivatives, to build a 6-DOF flight simulation model for crosswind landing conditions.

References

[1] EREA, Future Sky, Safety and Prevention, https://urldefense.com/v3/__https://futuresky.eu/themes/safety__;!!K7l7YuZ3_aFnun0eduI!mEdIald1O28Zg2PzamaOuaJZFnITcQyXxG-zme9jyZ6ISKYhCIqqKkTEN8X_05Meoi2GotHSAVGsLwQ0rRDuJSMo$ [last accessed Sep 2023].

[2] SkyBrary, Statistical Summary of Commercial Jet Airplane Accidents Worldwide Operations 1959-2015, July 2016, https://urldefense.com/v3/__https://skybrary.aero/sites/default/files/bookshelf/3811.pdf__;!!K7l7YuZ3_aFnun0eduI!mEdIald1O28Zg2PzamaOuaJZFnITcQyXxG-zme9jyZ6ISKYhCIqqKkTEN8X_05Meoi2GotHSAVGsLwQ0rVSRj_xR$

[3] Flight Safety Foundation, Approach-and-Landing Accident Reduction (ALAR) Briefing Note: 8.7 — Crosswind Landing. Flight Safety Foundation, Flight Safety Digest, 2000, https://urldefense.com/v3/__https://flightsafety.org/files/alar_bn8-7-crosswind.pdf__;!!K7l7YuZ3_aFnun0eduI!mEdIald1O28Zg2PzamaOuaJZFnITcQyXxG-zme9jyZ6ISKYhCIqqKkTEN8X_05Meoi2GotHSAVGsLwQ0rYx5fy-L$

[4] Hoak, D.E. The USAF Stability and Control DATCOM, TR-83-3048, 1960.

[5] Flaig, A. Results of wind tunnel ground effect measurements on Airbus A320 using turbine power simulation and moving tunnel floor techniques, AIAA-90-1427, 16th Aerodynamic Ground Testing Conference, 1966, https://doi.org/10.2514/6.1990-1427

[6] Deng, N. and Agarwal, R.K. Numerical simulation of DLR-F6 wing-body flow field in ground effect, *Comput. Fluids*, 2022, https://doi.org/10.1016/j.compfluid.2022.105576

[7] Doig, G. and Barber, T.J. Considerations for numerical modeling of inverted wings in ground effect, *AIAA J.*, 2011, **49**, pp 2330–2333, https://doi.org/10.2514/1.J051273

[8] Mahon, S. and Zhang, X. Computational analysis of pressure and wake characteristics of an aerofoil in ground effect, *J. Fluids Eng.*, 2005, **127**, pp 290–298, https://doi.org/10.1115/1.1891152

[9] Ahmed, M.R., Takasaki, T. and Kohama, Y. Aerodynamics of a NACA 4412 airfoil in ground effect, *AIAA J.*, 2007, **45**, pp 37–47, https://doi.org/10.2514/1.23872

[10] Partha, M. and Balakrishnan, N. Discrete vortex method-based model for ground-effect studies, *AIAA J.*, 2014, **52**, (12), pp 2817–2828, https://urldefense.com/v3/__https://doi.org/10.2514/1.J052920__;!!K7l7YuZ3_aFnun0eduI!mEdIald1O28Zg2PzamaOuaJZFnITcQyXxG-zme9jyZ6ISKYhCIqqKkTEN8X_05Meoi2GotHSAVGsLwQ0rVtEMK0i$

[11] Xuguo, Q., Peiqing, L. and Qiulin, Q. Aerodynamics of a multi-element airfoil near ground, *Tsinghua Sci. Tecnhol.*, 2014, **14**, (2), pp 94–99, https://ieeexplore.ieee.org/stamp/stamp.jsp?arnumber=6075572

[12] Sereez, M. and Zaffar, U. Dynamic stall on high-lift airfoil 30P30N in ground proximity, *Open J. Fluid Dyn.*, 2021, **11**, (1), pp 135–152, https://doi.org/10.4236/ojfd.2021.113008

[13] Hoak, D.E. and Finck, R.D. USAF Stability and DAR 303, Flight Safety Digest, 1974.

[14] Kemp, W.B., Vernerd Jr., E. and Phillips, W.P. Ground Effects related to Landing of Airplanes with Low-Aspect Ratio Wings, *NASA TN-D-3583*, 1966, https://urldefense.com/v3/__https://ntrs.nasa.gov/api/citations/19660028848/downloads/19660028848.pdf__;!!K7l7YuZ3_aFnun0eduI!mEdIald1O28Zg2PzamaOuaJZFnITcQyXxG-zme9jyZ6ISKYhCIqqKkTEN8X_05Meoi2GotHSAVGsLwQ0rbzMU2wk$

[15] Hermans, C. and Hegen, S. DNW innovations in wind tunnel testing: new moving belt system for Large Low speed Facility, *CEAS Aeronaut. J.*, 2018, **9**, pp 283–290, https://doi.org/10.4236/ojfd.2021.113008

[16] Lacy D.S. and Clark, A.M. Definition of initial landing and takeoff reference configurations for the High Lift Common Research Model (CRM-HL), AIAA 2020-2771, 2020, https://doi.org/10.2514/6.2020-2771

[17] Vassberg, J. A unified baseline grid about the common research model wing/body for the fifth AIAA CFD drag prediction workshop, *AIAA J.*, 2011, https://doi.org/10.2514/6.2011-3508

[18] AIAA, High Lift Prediction Workshop, https://urldefense.com/v3/__https://hiliftpw.larc.nasa.gov__;!!K7l7YuZ3_aFnun0eduI!mEdIald1O28Zg2PzamaOuaJZFnITcQyXxG-zme9jyZ6ISKYhCIqqKkTEN8X_05Meoi2GotHSAVGsLwQ0rWEaHs-S$ last accessed 8 June 2022

[19] Sereez, M., Abramov, N.B. and Goman, M.G. Impact of Ground Effect on lateral directional stability during take-off and landing, *Open J. Fluid Dyn.*, 2018, **8**, (1), pp 1–14, https://doi.org/10.4236/ojfd.2018.81001

[20] AIAA, Drag Prediction Workshop 4, https://urldefense.com/v3/__https://aiaa-dpw.larc.nasa.gov/Workshop4__;!!K7l7YuZ3_aFnun0eduI!mEdIald1O28Zg2PzamaOuaJZFnITcQyXxG-zme9jyZ6ISKYhCIqqKkTEN8X_05Meoi2GotHSAVGsLwQ0rew7LOeX$ [last accessed 1 June 2022].

[21] Evans, A.N., Lacy, D.S., Smith, I. and Rivers, M.B. Test summary of the NASA high-lift common research model half-span at QinetiQ 5-metre pressurized low- speed wind tunnel, AIAA 2020-2770, June 2020. https://doi.org/10.2514/6.2020-2770

[22] Chen, G., Xiong, O., Morris, P., Paterson, E., Sergeev, E. and Wang, Y. OpenFOAM for computational fluid dynamics, *Not. AMS*, 2014, **61**, (4), pp 354–363.

[23] Siemens Digital Industries Software, Simcenter STAR-CCM+ User Guide, version 2021.1, *Adaptive Mesh Refinement for Overset Meshes*, 2021, pp 3067–3070.

[24] Spalart, P.R. and Allmaras, S.R. A one-equation turbulence model for aerodynamic flows, 30th Aerospace Sciences Meeting and Exhibit, 1992, https://doi.org/10.2514/6.1992-439

[25] Venkatakrishnan, V. On the accuracy of limiters and convergence to steady-state solutions, 31st Aerospace Sciences Meeting, June 1993, https://doi.org/10.2514/6.1993-880

[26] Heffley, R.K. and Jewell, W.F. Definition of Aircraft Handling Qualities Data, NASA CR-2144, December 1972.

[27] EEC high performance cluster, Zeus HPC, 2022, https://urldefense.com/v3/__https://hpc.coventry.domains/links/zeus-hpc/__;!!K7l7YuZ3_aFnun0eduI!mEdIald1O28Zg2PzamaOuaJZFnITcQyXxG-zme9jyZ6ISKYhCIqqKkTEN8X_05Meoi2GotHSAVGsLwQ0rQKF_WQU$ [last accessed 25 June 2022].